AGU PUBLICATIONS

JGR

Journal of Geophysical Research: Oceans

RESEARCH ARTICLE

10.1002/2017JC012844

Special Section:
The Southern Ocean Carbon and Climate Observations and Modeling (SOCCOM) Project: Technologies, Methods, and Early Results

Revisiting Ocean Color algorithms for chlorophyll *a* and particulate organic carbon in the Southern Ocean using biogeochemical floats

Nils Haëntjens[1], Emmanuel Boss[1], and Lynne D. Talley[2]

[1]School of Marine Sciences, University of Maine, Orono, Maine, USA, [2]Scripps Institution of Oceanography, University of California, San Diego, La Jolla, California, USA

Abstract The Southern Ocean (SO) ecosystem plays a key role in the carbon cycle by sinking a major part (43%) of the ocean uptake of anthropogenic CO_2, and being an important source of nutrients for primary producers. However, undersampling of SO biogeochemical properties limits our understanding of the mechanisms taking place in this remote area. The Southern Ocean Carbon and Climate Observations and Modeling (SOCCOM) project has been deploying a large number of autonomous biogeochemical floats to study the SO (as of December 2016, 74 floats out of 200 have been deployed). SOCCOM floats measurements can be used to extend remote sensing chlorophyll *a* (chl *a*) and particulate organic carbon (POC) products under clouds or during the polar night as well as adding the depth dimension to the satellite-based view of the SO. Chlorophyll *a* concentrations measured by a sensor embedded on the floats and POC concentrations derived from backscattering coefficients were calibrated with samples collected during the floats' deployment cruise. Float chl *a* and POC were compared with products derived from observations of MODIS and VIIRS sensors. We find the Ocean Color Index (OCI) global algorithm to agree well with the matchups (within 9%, on average, for the Visible Infrared Imaging Radiometer Suite (VIIRS) and 12%, on average, for the Moderate Resolution Imaging Spectroradiometer *Aqua* (MODIS)). SO-specific algorithms estimating chl *a* are offset by ~45% south of the Sea Ice Extent Front (~60°S). In addition, POC estimates based on floats agree well with NASA's POC algorithm.

Key Points:
- Validation of remote sensing algorithms with biogeochemical profiling floats
- Ocean Color Index global algorithm performs well in the Southern Ocean
- Ocean Color POC agrees well with floats estimates in the Southern Ocean

Correspondence to:
N. Haëntjens,
nils.haentjens@maine.edu

Citation:
Haëntjens, N., E. Boss, and L. D. Talley (2017), Revisiting Ocean Color algorithms for chlorophyll *a* and particulate organic carbon in the Southern Ocean using biogeochemical floats, *J. Geophys. Res. Oceans*, *122*, doi:10.1002/2017JC012844.

Received 28 FEB 2017
Accepted 22 JUN 2017
Accepted article online 5 JUL 2017

1. Introduction

The Southern Ocean (SO), the oceanic region between 30°S and Antarctica, occupies 30% of the world's oceans but plays a disproportionate role in their biogeochemistry: 43% of the ocean uptake of anthropogenic CO_2 is taken up in the SO [*Frölicher et al*., 2015] and it is the source of 75% of nutrients used by primary producers north of 30°S [*Sarmiento et al*., 2004]. In realization of its contributions and in light of the lack of year-round data, a consortium of scientists has built a profiling-float-based observatory equipped with state-of-the-art biogeochemical sensors.

The Southern Ocean Carbon and Climate Observations and Modeling (SOCCOM) is a six-year NSF-funded initiative that received additional funding from NOAA and NASA. SOCCOM floats, deployed in the SO, are typically equipped with CTD, nitrate, oxygen, and pH sensors, as well as sensors that measure light backscattered at 700 nm and chlorophyll *a* (chl *a*) fluorescence. The latter provides an opportunity to validate space-derived biogeochemical products from another spatially and temporally extensive observation system, Ocean Color (OC). While much of the SO can be observed by OC year around, the regions south of 55°S are not observed for several months of the year due to either low sun angle or absence of sunlight [*Behrenfeld et al*., 2016].

Since the launch of NASA's Coastal Zone Color Scanner (CZCS), OC has been used to derive biogeochemical parameters in the SO, in particular chl *a* and particulate organic carbon (POC). It has been found, however, that in the SO the globally derived empirical chl *a* algorithms are biased. *Mitchell and Holm-Hansen* [1991] and *Sullivan et al*. [1993] found a significant (factor of 2.4) underestimate of SO chl *a* by the global CZCS algorithm. *Dierssen and Smith* [2000] found a similar bias (underestimation of ~2) with the Sea-Viewing Wide Field-of-View Sensor's (SeaWiFS) algorithm. These studies were based on a large database of fluorometrically extracted chl *a*. *Mitchell and Kahru* [2009] and *Kahru and Mitchell* [2010] proposed an algorithm (SPGANT) for the Advanced Earth Observing Satellite (ADEOS), SeaWiFS, and the Moderate Resolution

Imaging Spectroradiometer *Aqua* (MODIS) satellites, to correct this SO bias. *Guinet et al*. [2013] have found, using chl *a* fluorometers mounted on elephant seals calibrated with High-Performance Liquid Chromatography (HPLC), that the standard algorithms underestimate chl *a* by ~2 times with MODIS. Finally, *Johnson et al*. [2013] have found using a large HPLC-based chl *a* data set (~1400 samples) that NASA's SeaWiFS and MODIS algorithms underestimated chl *a* by a factor of about 3 and 4, respectively, at latitudes south of 35°S and between 20°E and 160°E. Species composition, physiology, and particulate composition were invoked to explain this underestimation [see the review of *Dierssen*, 2010]. Note, however, that *Marrari et al*. [2006] observed no significant bias between SeaWiFS' chl *a* and HPLC chl *a*.

The remoteness of the SO and the limited ability to cover its extent with research expeditions have limited the exercise of satellite and in situ matchups to selected regions and seasons. For example, the bulk (>95%) of the data in *Johnson et al*. [2013] was collected in a narrow corridor south of Tasmania, located between 140°E and 150°E. In *Mitchell and Kahru* [2009], the in situ data were collected from 1997 to 2008, primarily during austral summers in the Scotia Sea. *Guinet et al*. [2013] covered several seasons (December 2007 to February 2011) but were limited to the region south of the Indian Ocean. Wide areas such as the south Pacific Ocean and the southeastern Atlantic Ocean had no matchups in those studies.

Here we use a recently assembled HPLC and POC data set, collected in conjunction with SOCCOM profiling-float deployments on five different SO cruises, to evaluate the performance of NASA's MODIS and Visible Infrared Imaging Radiometer Suite (VIIRS) global algorithms. MODIS and VIIRS are polar orbitting multispectral satellites with visible and infrared detectors to measure top of the atmosphere (TOA) radiance. The products used are derived from the TOA radiance by applying an atmospheric correction [*Mobley et al*., 2016] and application of community developed algorithms by the NASA Ocean Biology and Biogeochemistry group. In situ HPLC and POC data are used to calibrate sensors (chl *a* fluorescence and scattering around an angle in the back direction) deployed on profiling floats [*Johnson et al*., 2017]. These calibrated sensors, in turn, are used to assemble a float-OC matchup data set throughout the SO. With this data set, we find no statistically significant bias of NASA's MODIS and VIIRS algorithms for chl *a* or POC.

2. Methods

2.1. Float Products

Pre-SOCCOM and SOCCOM float profiles from the FloatViz archival data set of 28 November 2016 are used in this study (Table 1). The in situ data used to calibrate the float sensors were collected during the cruises: P16S, A12, SOTS, OOISO, and P15S (Table 2).

The full description of data processing and quality control is provided in *Johnson et al*. [2017]. Here we provide a shorthand version for the sake of completeness. The chl *a* fluorometers raw data are transformed to engineering units using the manufacturer calibration coefficients, the dark counts are adjusted to avoid signal contamination by fluorescent colored dissolved organic material [*Xing et al*., 2017], and the profiles are corrected for nonphotochemical quenching [*Sackmann et al*., 2008; *Xing et al*., 2011]. The chl *a*:fluorescence ratio is adjusted for all the floats together, regressing chl *a* fluorescence from floats with total chl *a* from HPLC samples taken during float deployment. Two regressions are shown in *Johnson et al*. [2017]: a linear regression (slope of 6.44) as commonly used in the literature, and a power law fit. Since the power law fit performs better relative to the HPLC data set and uses the same number of parameters, it is used here to derive chl *a* from the float measurements. The average error for chl *a* estimated from floats is the larger of 0.12 mg m^{-3} or 37% (and the relationship is $\text{chl}\,a_{HPLC} = 0.21(\pm 0.02) \times \text{chl}\,a_{float}^{0.714(\pm 0.242)}$ with standard deviation of the regression coefficients in the parentheses.

The volume scattering function (VSF) arround one angle in the backward direction measured by the backscattering sensor is computed using the calibration coefficients of the manufacturer (if darks measured before the deployment of the float are available, they are used instead of the manufacturers' darks). The VSF of seawater [*Zhang et al*., 2009] is removed from the VSF at the measured angle in the back direction, which in turn is converted to particulate backscattering (b_{bp}) with the conversion factor from *Sullivan et al*. [2013]. An empirical relationship between b_{bp} and POC is built by regressing the POC samples taken during float deployment with the b_{bp} measured during the first profile of the floats [*Johnson et al*., 2017]. The average error for estimated POC from floats is the larger of 35 mg m^{-3} or

Table 1. List of Floats and Associated Bio-Optical Sensor From the FloatViz Archival Data Set of 28 November 2016[a]

UW Id[b]	WMO Id[c]	Sensor Model	Sensor SN	# Profiles	Zone	Date First Profile	Date Last Profile
0037	5904475	MCOMS	0015	79	STZ	05-Dec-2014 21:51:00	26-Nov-2016 00:33:00
0068	5903717	FLBBAP2	1550	243	SAZ, SIZ	19-Feb-2012 08:08:00	31-May-2016 03:24:00
0506	5904670	MCOMS	0109	8	SIZ	24-Jan-2016 08:24:00	03-Apr-2016 15:06:00
0507	5904671	MCOMS	0114	29	SIZ	15-Feb-2016 15:53:00	22-Nov-2016 01:25:00
0508	5904476	MCOMS	0032	54	SAZ, PAZ	09-Dec-2014 14:17:00	29-Feb-2016 04:35:00
0509	5904477	MCOMS	0017	17	PAZ, SIZ	13-Dec-2014 01:11:00	02-Jun-2015 06:56:00
0510	5904686	MCOMS	0115	27	PAZ, SIZ	25-Feb-2016 15:45:00	22-Nov-2016 19:52:00
0511	5904478	MCOMS	0034	4	SIZ	18-Dec-2014 16:32:00	17-Jan-2015 20:15:00
0564	5904687	MCOMS	0113	8	SIZ	23-Feb-2016 12:39:00	02-May-2016 20:49:00
0566	5904766	MCOMS	0118	20	PAZ	16-May-2016 04:29:00	22-Nov-2016 04:11:00
0571	5904673	MCOMS	0059	20	PAZ	12-May-2016 17:42:00	19-Nov-2016 03:41:00
6091	5904179	FLBB	3144	95	SAZ, PAZ	27-Mar-2014 05:11:00	20-Nov-2016 23:51:00
6967	5903612	FLBBAP2	2100	221	STZ, SAZ	11-Dec-2011 22:53:00	21-Feb-2016 17:08:00
6968	5903718	FLBBAP2	1738	250	SAZ	06-Mar-2012 01:44:00	21-Sep-2015 12:05:00
7552	5903593	FLBBAP2	1890	250	STZ, SAZ	15-Mar-2012 03:35:00	28-Oct-2015 08:56:00
7557	5904181	FLBB	3146	15	SAZ	28-Mar-2014 18:30:00	19-Aug-2014 21:06:00
7567	5904182	FLBB	3145	38	SAZ	10-Apr-2014 06:06:00	26-Apr-2015 19:15:00
7613	5904180	FLBB	3148	78	SAZ	31-Mar-2014 19:35:00	31-May-2016 12:56:00
7614	5904183	FLBB	3147	75	SAZ	01-Apr-2014 17:04:00	02-May-2016 10:04:00
7619	5904105	FLBBAP2	1887	182	SAZ, PAZ, SIZ	03-Mar-2013 07:22:00	15-Aug-2016 23:24:00
7620	5904104	FLBBAP2	1888	207	SAZ, PAZ, SIZ	04-Mar-2013 12:57:00	24-Nov-2016 16:54:00
7652	5904467	FLBB	3291	53	SAZ, SIZ	14-Dec-2014 19:03:00	02-Jun-2016 01:09:00
8514	5904470	FLBB	2993	67	SAZ	26-Mar-2015 20:17:00	23-Nov-2016 14:00:00
9031	5904396	FLBB	3306	129	SAZ	12-Apr-2014 03:35:00	03-Nov-2016 23:27:00
9091	5904184	FLBB	3308	95	SAZ	03-Apr-2014 23:12:00	27-Nov-2016 09:22:00
9092	5904185	FLBB	3173	94	SAZ	07-Apr-2014 23:03:00	22-Nov-2016 21:07:00
9094	5904471	FLBB	3641	51	SAZ, SIZ	21-Dec-2014 12:49:00	30-May-2016 20:27:00
9095	5904188	FLBB	3307	114	SAZ	15-Apr-2014 07:13:00	26-Nov-2016 09:40:00
9096	5904469	FLBB	3327	70	SAZ, PAZ	11-Dec-2014 12:34:00	23-Nov-2016 09:05:00
9099	5904468	FLBB	3178	49	SIZ	19-Jan-2015 22:11:00	28-May-2016 15:19:00
9125	5904397	FLBB	3309	49	SAZ, SIZ	22-Jan-2015 05:31:00	31-May-2016 01:16:00
9254	5904395	FLBB	2935	131	SAZ	21-Apr-2014 18:56:00	26-Nov-2016 02:01:00
9260	5904473	FLBB	3640	64	SAZ, PAZ	28-Jan-2015 07:05:00	09-Nov-2016 11:13:00
9275	5904472	FLBB	3643	42	SAZ	18-Jan-2015 21:56:00	27-Mar-2016 07:10:00
9313	5904474	FLBB	3646	87	STZ, SAZ, PAZ	07-Dec-2014 23:50:00	24-Nov-2016 04:15:00
9600	5904688	FLBB	3811	26	STZ, SAZ	06-Mar-2016 01:45:00	19-Nov-2016 16:29:00
9602	5904684	FLBB	3655	25	PAZ	28-Feb-2016 22:15:00	17-Nov-2016 18:51:00
9631	5904677	FLBB	3686	28	SAZ, PAZ	01-Apr-2016 17:22:00	25-Nov-2016 00:24:00
9632	5904763	FLBB	3682	19	SAZ	19-May-2016 10:24:00	20-Nov-2016 13:06:00
9634	5904693	FLBB	3809	19	SAZ	20-May-2016 18:33:00	23-Nov-2016 06:08:00
9637	5904682	FLBB	3810	27	SAZ, PAZ	02-Mar-2016 03:24:00	26-Nov-2016 21:28:00
9645	5904676	FLBB	3688	29	SAZ, PAZ	18-Jan-2016 05:38:00	20-Nov-2016 18:14:00
9646	5904661	FLBB	3806	33	SAZ	29-Dec-2015 05:25:00	24-Nov-2016 22:22:00
9650	5904683	FLBB	3685	27	SAZ, PAZ	03-Mar-2016 23:57:00	28-Nov-2016 00:56:00
9652	5904660	FLBB	3803	32	SAZ	07-Jan-2016 19:29:00	24-Nov-2016 09:31:00
9657	5904659	FLBB	3808	32	SAZ	08-Jan-2016 09:14:00	24-Nov-2016 02:37:00
9660	5904761	FLBB	3807	19	SAZ	18-May-2016 06:02:00	19-Nov-2016 17:01:00
9744	5904678	FLBB	3645	29	SAZ	07-Apr-2016 22:47:00	21-Nov-2016 11:36:00
9757	5904679	FLBB	3684	31	PAZ	19-Jan-2016 04:04:00	25-Nov-2016 16:46:00
9762	5904765	FLBB	3804	18	SAZ	31-May-2016 20:49:00	23-Nov-2016 20:02:00

[a]The oceanic zones are shown on the map Figure 1 and their acronyms stands for sea ice zone (SIZ), Polar Antarctic Zone (PAZ), Subantarctic Zone (SAZ), and the Subtropical Zone (STZ).
[b]University of Washington identification number, used in FloatViz.
[c]World Meteorological Organization identification number.

47% (and the relationship is $POC = 3.12\times10^{4}(\pm2.47\times10^{3})\times b_{bp}(700)+3.0(\pm6.8)$ with standard deviation of the regression coefficients in the parentheses).

2.2. Comparison With Remote Sensing

Chl *a* and POC are derived from remote sensing reflectance (R_{rs}) for both MODIS and VIIRS sensors reprocessing 2014.0 [*NASA Goddard Space Flight Center et al.*, 2014, 2015]. The matchups with float profiles are broadly distributed around Antarctica, mainly south of 45°S as presented in Figure 1, and cover multiple seasonal cycles.

Ocean Color Index (OCI) [*Hu et al.*, 2012], the latest global chl *a* algorithm from NASA, is compared to two algorithms specific to the Southern Ocean: SPGANT version 4 [*Mitchell and Kahru*, 2009; *Kahru and Mitchell*,

Table 2. List of Cruises During Which HPLC and POC Samples Were Collected and Used to Calibrate Float Sensors

Cruise	Expedition Code	# HPLC Samples	# POC Samples	# Float Deployed	Latitude Range	Longitude Range	Sampling Period
P16S	320620140320	80	61	12	67°S–15°S	174°E–149°W	Mar–May 2014
A12	06AQ20141202	37	38	12	70°S–37°S	9°W–13°E	Dec 2014 to Jan 2015
SOTS	096U20150321	0	14	1	47°S–46°S	141°E–144°E	Mar 2015
OOISO	320620151206	4	4	3	54°S–53°S	89°W–80°W	Dec 2015
P15S	096U20160426	20	20	10	66°S–46°S	171°W–169°W	May 2016

2010] and *Johnson et al*. [2013] (referred as J13, implementation in Table 3) using matchups of MODIS or VIIRS images with float profiles. OCI is a blend of the band ratio algorithm OCx (OC3M or OC3V, for MODIS and VIIRS, respectively) and the color index (CI) algorithm of *Hu et al*. [2012]; the algorithm transitions between $0.15 < [\text{chl}\,a] < 0.20$ mg m^{-3} (CI at low [chl *a*] and OCx at high [chl *a*]). This algorithm was not used as a default OC algorithm at the time when SPGANTv4 and J13 were built. SPGANTv4 [*Mitchell and Kahru*, 2009] is used in conjunction with OC3M: for $[\text{chl}\,a] <= 0.07$ OC3M is used, between $0.07 < [\text{chl}\,a] < 0.13$ a linear transition between the two algorithms is applied, and for $[\text{chl}\,a] > = 0.13$ SPGANTv4 is used [*Kahru and Mitchell*, 2010]. The algorithm of *Stramski et al*. [2008] is used for POC.

In order to maximize the quality of the comparison between floats and OC, "good quality" matchups are required. *Bailey and Werdell* [2006] defined these as: a narrow time window (±3 h) between in situ and satellite records, computed from the mean of a 5 × 5 pixel box centered on the in situ measurement, and a good atmospheric correction (mask pixels with default level 3 flags on; a description of the flags used by OC is available at: https://oceancolor.gsfc.nasa.gov/atbd/ocl2flags/). For our data set, this resulted in only four matchups with MODIS products. Several factors might explain this: the floats' surface time is not synchronized with NASA satellites' overpasses, cloud coverage is high all year long in the Southern Ocean, the polar night, or high solar zenith angle (>70°) during several months.

Widening the spatial and temporal window increases the number of matchups at the possible cost of quality, but as mentioned in the report from *IOCCG* [2011], optical data exhibit large spatial and temporal correlations making them useful for matching-up beyond the narrow window specified above. A spatial correlation analysis (Figure 2) shows that we can increase the number of matchups significantly with a relatively small decrease in correlation by averaging products within an 8 km radius circle and a 24 h window, keeping the same level 2 flags criteria as the "good quality" matchups.

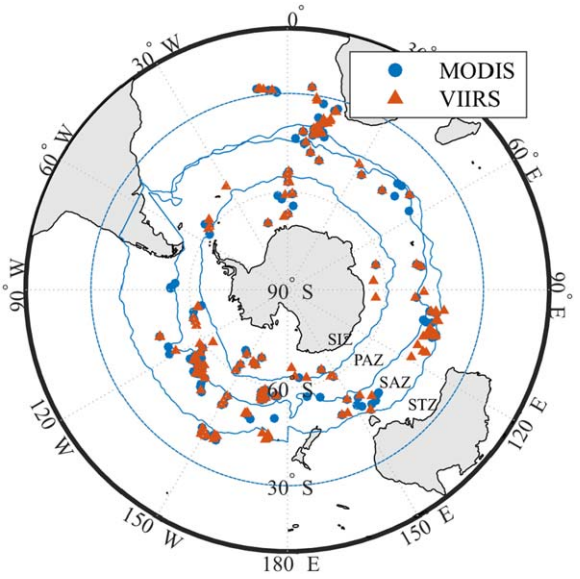

Figure 1. SOCCOM and pre-SOCCOM float and Ocean Color (OC) matchup locations (MODIS in blue circles and VIIRS in red triangles). The acronyms of each region of the Southern Ocean stands for sea ice zone (SIZ), Polar Antarctic Zone (PAZ), Subantarctic Zone (SAZ), and the Subtropical Zone (STZ).

To account for vertical structure of the water column, we optically weight chl *a* and POC (equation (1)) from floats according to *Gordon and Clark* [1980] [*Werdell and Bailey*, 2005; *Mueller et al*., 2003; *Zaneveld et al*., 2005],

$$<\text{chl}\,a> = \frac{\sum e^{-2K_d z}\,\text{chl}\,a_{float}(z)}{\sum e^{-2K_d z}} \qquad (1)$$

with K_d as the diffuse attenuation coefficient of downwelling irradiance at 490 nm, derived from satellite measurements (with KD2M and KD2V for MODIS and VIIRS, respectively), and *z* as the depths of the float measurements.

2.3. Matchup Fits and Associated Statistics

Of primary interest is the slope of the linear type II regression (reduced major axis, defined by *Ricker* [1973]). The regression's standard deviation (std) of both the slope and offset

Table 3. Chlorophyll *a* and POC Algorithms Applied to Remote Sensing Reflectance

Product	Sensor	Algorithm	Equations
chl *a*	MODIS	OCI	Merged OC3M band ratio algorithm with color index (CI) of *Hu et al.* [2012]
chl *a*	MODIS	J13[a]	$R_{sw}=log_{10}\left(\frac{\max(R_{rs}(443),R_{rs}(488))}{R_{rs}(547)}\right)$ $\text{chl}\,a_{J13}=10^{0.6994-2.0384R_{sw}-0.4656R_{sw}^2+0.4337R_{sw}^3}$
chl *a*	MODIS	SPGANTv4	$L_{wn}(\lambda)=\frac{F_0(\lambda)\times R_{rs}(\lambda)}{\pi}$ $R=log_{10}\left(\frac{\max(L_{wn}(443),L_{wn}(488))}{L_{wn}(547)}\right)$ $\text{chl}\,a_{SPGANTv4}=10^{0.5514-2.2434R+0.0746R^2-0.0095R^3-0.7790R^4}$ blended with OC3M [*Kahru and Mitchell*, 2010]
chl *a*	VIIRS	OCI	Merged OC3V band ratio algorithm with color index (CI) of *Hu et al.* [2012]
chl *a*	VIIRS	J13[a]	$R_{sw}=log_{10}\left(\frac{\max(R_{rs}(410),R_{rs}(443),R_{rs}(486))}{R_{rs}(551)}\right)$ $\text{chl}\,a_{J13}=10^{0.6736-2.0714R_{sw}-0.4939R_{sw}^2+0.4756R_{sw}^3}$
POC	MODIS	S08[b]	$POC=203\times\left(\frac{R_{rs}(443)}{R_{rs}(547)}\right)^{-1.034}$
POC	VIIRS	S08[b]	$POC=203\times\left(\frac{R_{rs}(443)}{R_{rs}(551)}\right)^{-1.034}$

[a] *Johnson et al.* [2013].
[b] *Stramski et al.* [2008].

are computed following the treatment of *Ricker* [1973] for a model I regression. The squared Pearson's linear correlation coefficient (r^2) indicates the proportion of variance explained by a linear dependence between two independent variables, and is defined by

$$\bar{x}=\frac{\sum_{i=1}^{n}x_i}{n}\quad \bar{y}=\frac{\sum_{i=1}^{n}y_i}{n} \tag{2}$$

$$r^2=\left(\frac{\sum_{i=1}^{n}(x_i-\bar{x})(y_i-\bar{y})}{\sqrt{\sum_{i=1}^{n}(x_i-\bar{x})^2\times\sum_{i=1}^{n}(y_i-\bar{y})^2}}\right)^2 \tag{3}$$

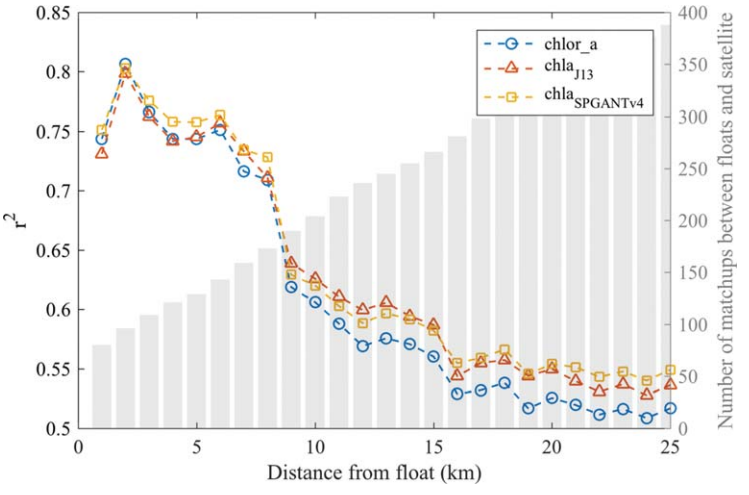

Figure 2. Spatial correlation between float and MODIS chlorophyll *a* (chl *a*). The histogram represents the number of satellite images available for a given radius around the position at which a float surfaced and within ±24 h. The correlation coefficient (r^2) between floats and MODIS chl *a* varies as a function of the radius of the disk in which satellite pixels are averaged. Algorithms used to derive chl *a* concentration from remote sensing reflectance are OCI (chlor_a, blue circles), J13 (chl a_{J13}, red triangles), and SPGANTv4 (chl $a_{SPGANTv4}$, yellow squares). Similar results are observed with VIIRS.

with n as the number of matchups, x and y the two data sets (in our case, one is the product from the float (y) and the other is the product from the satellite (x)). The root-mean-square deviation (*RMSD*) was defined by

$$RMSD=\sqrt{\frac{\sum_{i=1}^{n}(y_i-x_i)^2}{n}} \tag{4}$$

The root-mean-square relative deviation (*RMSRD*) is defined by

$$RMSRD=\sqrt{\frac{\sum_{i=1}^{n}\left(\frac{y_i-x_i}{y_i}\right)^2}{n}} \tag{5}$$

The ratio from the RMSRD might be very large due to uncertainties in both float

and OC data sets which bias the relative deviation. For this reason, a root-mean-square unbiased relative deviation (RMSURD) is also used, as defined by *Hu et al*. [2012]:

$$RMSURD=\sqrt{\frac{\sum_{i=1}^{n}\left(\frac{y_i-x_i}{0.5\times(x_i+y_i)}\right)^2}{n}} \tag{6}$$

The mean absolute error (ME) and mean unbiased relative error (MURE) are defined by

$$ME=\frac{\sum_{i=1}^{n}(y_i-x_i)}{n} \tag{7}$$

$$MURE=\frac{\sum_{i=1}^{n}\left(\frac{y_i-x_i}{0.5\times(x_i+y_i)}\right)}{n} \tag{8}$$

3. Results

We compare the float-based estimates of chl *a* and POC with those derived by remote sensing algorithms, using float and OC matchups. For chl *a* concentrations, we find that the global OCI algorithm performs better than the SO-specific algorithms SPGANTv4 and J13 (Table 4 and Figure 3). In fact, the frequency distribution of the satellite data overlaps well with the frequency distribution of float observations (Figures 3c and 3f). The OCI algorithm underestimates, on average, the [chl *a*] by 9% for VIIRS whereas it overestimates it by 12% for MODIS. SPGANTv4 and J13 overestimate chl *a*, on average, by a factor of 2 for all regions combined.

OCI's mean absolute deviation is on the order of 0.1 mg m^{-3} and is significantly lower (by a factor between 3 and 4) than J13 and SPGANTv4. The relative deviation exhibits the same trend. These metrics suggest that the OCI algorithm performs better than J13 and SPGANTv4 (Table 4). However, the unbiased relative deviation (RMSURD) between the float and OC chl *a* of this study is higher (∼45%) than for the matchups used to build the relationship of the color index (CI) algorithm of *Hu et al*. [2012] (32.7% for CI and 25.5% for OC3M). The deviation from the in situ data (RMSD and RMSRD) for MODIS and VIIRS sensors using J13 and SPGANTv4 algorithms was not reported in the relevant publications.

To study the biases, we analyze matchups as a function of the four distinct biogeochemical provinces of the SO. These regions are defined through the application of the *Orsi et al.* [1995] criteria to a ten-year Argo temperature and salinity climatology [*Roemmich and Gilson*, 2009] (A. Gray and S. Bushinsky, personal communication, 2017). The regressions for the Subantarctic Zone (SAZ) and Polar Antarctic Zone (PAZ), south of the subtropical front (STF), and north of the mean 2014–2015 September sea ice extent, have a smaller slope (0.84 ± 0.10) compared with the areas north and south of those boundaries, the Subtropical Zone (STZ) and the sea ice zone (SIZ), where the regression is 1.00 ± 0.10. On the other hand, for the STZ, SAZ, and PAZ, no significant offset is observed, whereas in the SIZ chl *a* is underestimated (∼20%) by OCI. A

Table 4. Statistics of Regressions Between the Float Measurements and Satellite Observations[a]

Sensor	Algorithm	Slope Linear	Offset Linear	*n*	r^2 Linear	*RMSD* Linear	*RMSRD* Linear	*RMSURD* Linear	r^2 Log	*RMSD* Log	*RMSRD* Log	*RMSURD* Log
MODIS	OCI	0.88 (±0.04)	0.01 (±0.01)	173	0.67	0.11	0.73	0.45	0.58	0.21	1.55	0.40
MODIS	J13	0.35 (±0.02)	0.07 (±0.01)	173	0.66	0.43	1.74	0.74	0.60	0.36	5.59	342.00
MODIS	SPGANTv4	0.41 (±0.02)	0.05 (±0.01)	173	0.70	0.35	1.51	0.68	0.63	0.33	4.49	2.69
VIIRS	OCI	1.09 (±0.05)	−0.02 (±0.01)	203	0.61	0.10	0.61	0.44	0.50	0.20	0.73	0.44
VIIRS	J13	0.49 (±0.03)	0.05 (±0.01)	203	0.49	0.28	1.41	0.62	0.48	0.30	2.94	2.26
Both[b]	OCI	0.97 (±0.03)	−0.00 (±0.01)	376	0.63	0.10	0.67	0.45	0.54	0.20	1.18	0.43
MODIS	POC	0.94 (±0.06)	−11.47 (±5.08)	173	0.37	31.46	0.72	0.44	0.44	0.20	0.13	0.12
VIIRS	POC	1.15 (±0.07)	−14.30 (±5.41)	203	0.34	28.60	0.57	0.38	0.40	0.17	0.11	0.10
Both[b]	POC	1.05 (±0.05)	−12.85 (±3.79)	376	0.33	29.95	0.64	0.41	0.40	0.19	0.12	0.11

[a]The standard deviation of the regression coefficients are in parentheses. The statistics are presented with the same data in both linear and log space.
[b]Both MODIS and VIIRS satellites.

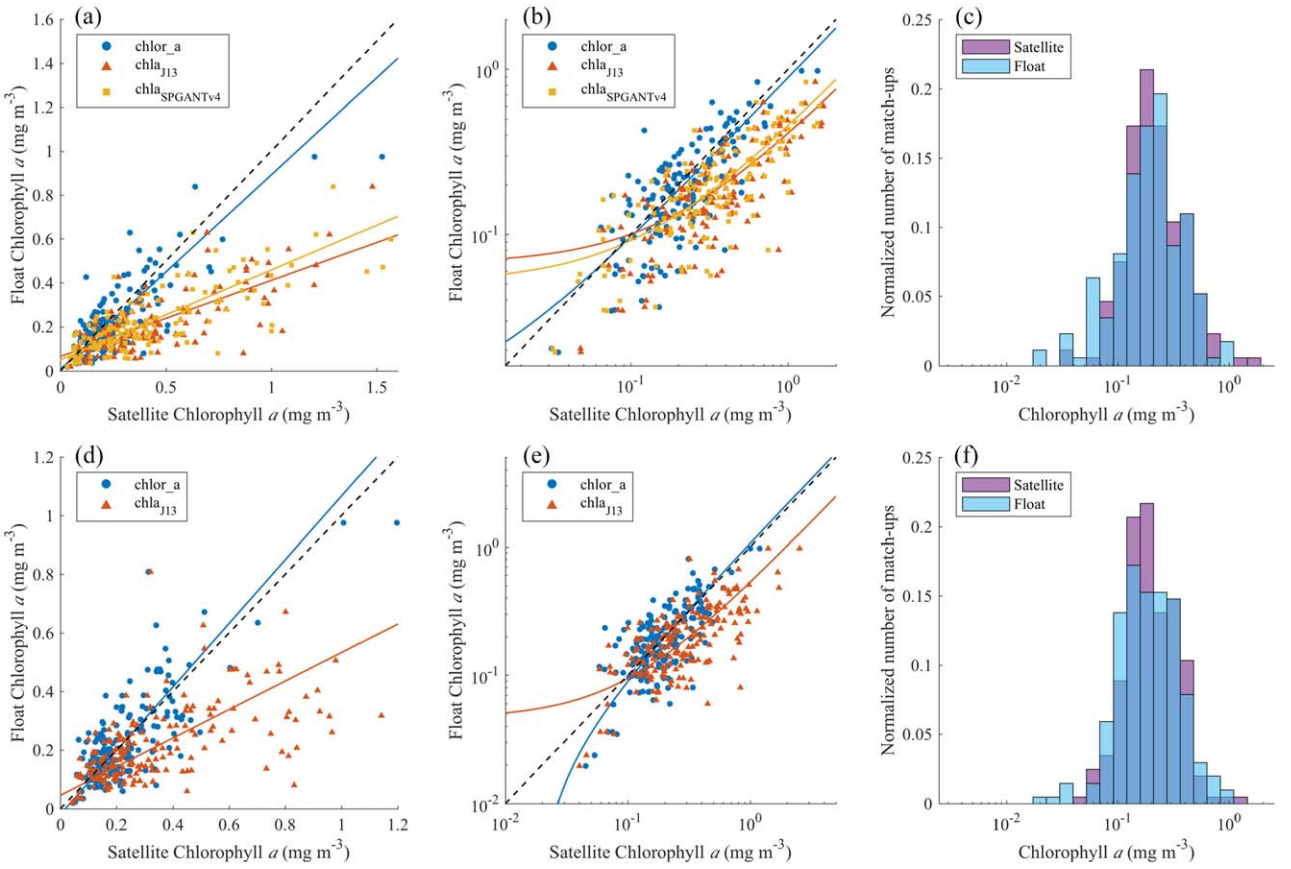

Figure 3. Chlorophyll *a* comparison in (a, d) linear space and (b, e) log space of the following chlorophyll *a* algorithms (Table 3): OCI (chlor_a, blue circles), J13 (chl $a_{J13,}$ red triangles), and SPGANTv4 (chl $a_{SPGANTv4,}$ yellow squares); for both (a–c) MODIS and (d–f) VIIRS. The frequency distribution of the float (transparent blue) and OCI (purple) chlorophyll *a* concentration are presented in Figures 3c and 3f. Statistics are presented in Table 4. Chlorophyll *a* from remote sensing is averaged within an 8 km radius circle.

similar study was conducted filtering the matchups by seasons, but no significant bias or offset are observed for any season. During the winter no matchups are available in the SIZ and significantly lower chl *a* values are observed in the other regions.

Since both OCI and SPGANT are blended algorithms, the matchups were analyzed for three ranges of chl *a* concentration: [chl *a*] $\leq$ 0.15 mg m^{-3}, 0.15 $<$ [chl *a*] $<$ 0.2 mg m^{-3}, and 0.2 $\leq$ [chl *a*] mg m^{-3} (Table 5). The same regression (linear type II) were used to conduct the analysis except that their intercept was forced to zero. At low chl *a* concentrations, both CI (from OCI) and OC3M (from SPGANT) have

Table 5. Statistics of Comparison Between the Float Measurements and Satellite Observations Grouped by Chlorophyll a Concentrations

Sensor	Algorithm	Subset (mg m^{-3})	*n*	Slope	*ME* (mg m^{-3})	*MURE* (Unitless)
Both[a]	OCI	ALL	376	0.98 (±0.03)	−0.01	−0.08
Both[a]	OCI	[chl *a*] $\leq$ 0.15	112	1.19 (±0.22)	0.02	0.01
Both[a]	OCI	0.15 $<$ [chl *a*] $<$ 0.2	80	1.08 (±0.53)	0.00	−0.05
Both[a]	OCI	0.2 $\leq$ [chl *a*]	184	0.94 (±0.05)	−0.03	−0.15
MODIS	OCI	ALL	173	0.94 (±0.04)	−0.02	−0.12
MODIS	OCI	[chl *a*] $\leq$ 0.15	46	1.08 (±0.36)	0.01	−0.07
MODIS	OCI	0.15 $<$ [chl *a*] $<$ 0.2	37	1.10 (±0.81)	0.01	−0.05
MODIS	OCI	0.2 $\leq$ [chl *a*]	90	0.90 (±0.06)	−0.05	−0.18
MODIS	SPGANTv4	ALL	173	0.53 (±0.02)	−0.22	−0.51
MODIS	SPGANTv4	[chl *a*] $\leq$ 0.15	28	1.03 (±0.26)	−0.00	−0.11
MODIS	SPGANTv4	0.15 $<$ [chl *a*] $<$ 0.2	15	0.96 (±1.37)	−0.01	−0.12
MODIS	SPGANTv4	0.2 $\leq$ [chl *a*]	130	0.50 (±0.03)	−0.28	−0.64

[a]Both MODIS and VIIRS satellites.

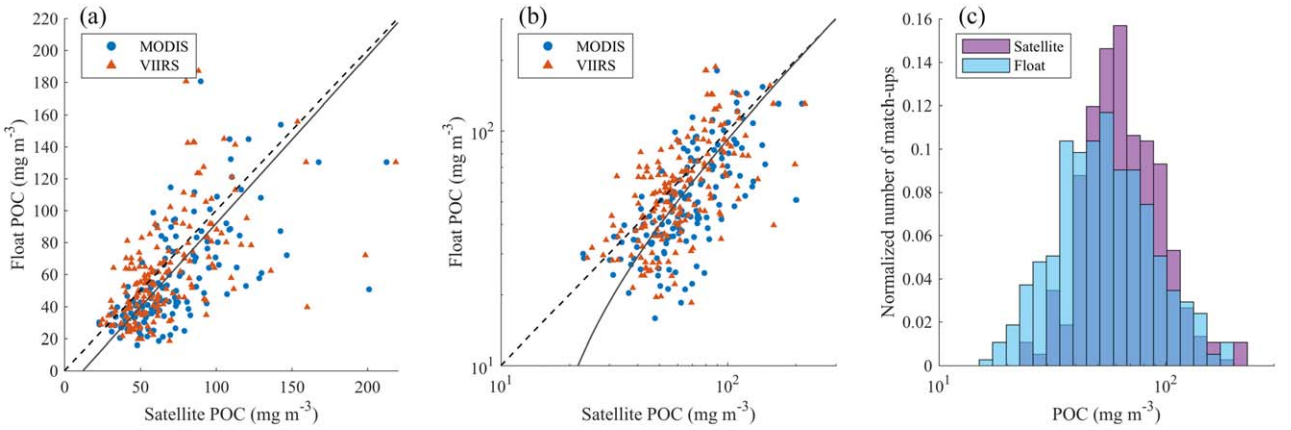

Figure 4. POC regressions between float and both satellite sensors (MODIS, blue circles; VIIRS, red triangles) using *Stramski et al*. [2008] (Table 3): (a) In linear space, (b) in log/log space, and (c) an histogram of the frequency distribution of the data (satellite in purple and float in transparent blue). Statistics are presented in Table 4. POC from remote sensing is averaged within an 8 km radius circle.

slope close to 1 (within 19%) and have no significant offset (<12%). At high chl *a* concentrations, OC3M (from OCI) performs significantly better than SPGANT, in fact the slope indicates that OC3M is overestimating [chl *a*] by 10% (which is within the uncertainty) whereas SPGANT overestimate it by 50%. Note that more low chl *a* concentration matchups are needed to quantify the improvement of CI versus OCx in the SO.

Float-based POC estimates agree well with NASA's algorithm but also exhibit a large spread (relatively low prediction capability) in matchups (Table 4 and Figure 4). The uncertainty of the POC for both sensors (Table 4) is very close to the one from the algorithm used [*Stramski et al*., 2008] which has an RMSD = 21.3 mg m^{-3}, RMSRD = 21.7%, $r^2 = 0.87$, for N = 53. This supports the consistency of this product across the globe and the SO.

4. Discussion

We find that the SO-specific chl *a* algorithms [*Mitchell and Kahru*, 2009; *Kahru and Mitchell*, 2010; *Johnson et al*., 2013] overestimate [chl *a*] concentration in the SIZ region where we expected them to perform better than OCI. The reason may be that the data sets used in the SO studies come from restricted seasons and regions in the SO, while our float-based data are spread wider geographically (South Pacific and South East Atlantic) and temporally (cover evenly several season cycles) in the SO (compare

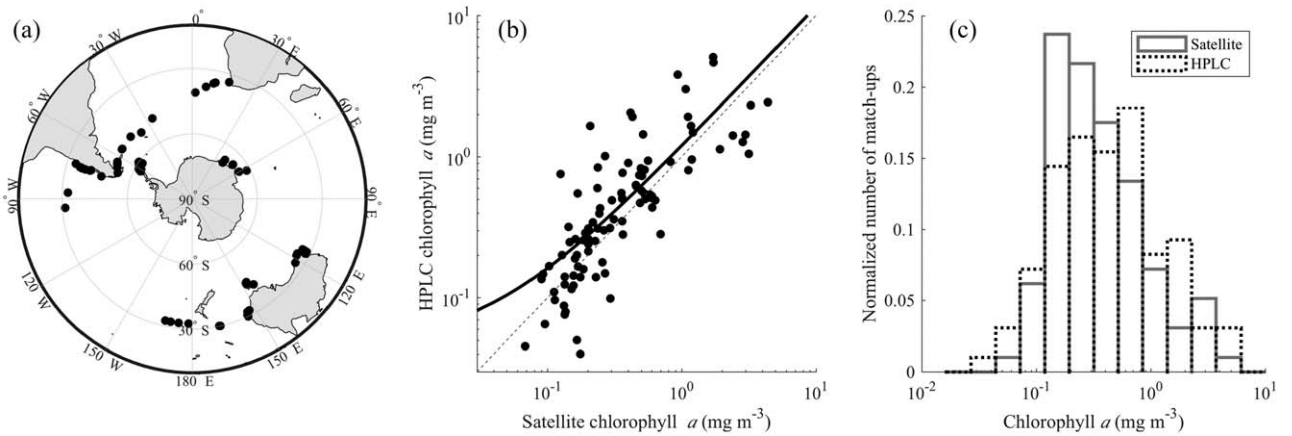

Figure 5. (left to right) (a) Map of area south of 30°S, (b) regression, and (c) histogram of the matchups between the SeaBASS database of in situ chlorophyll *a* from HPLC analysis and MODIS chlorophyll *a* from OCI. The regression plot is in log/log space, the dashed line corresponds to the 1:1 line, and the black line is a linear regression type II (chl a_{HPLC} = 1.15(±0.11)×chl a_{sat} + 0.05(±0.11). In linear space, RMSD = 0.78 mg m^{-3}, RMSRD = 0.70, RMSURD = 0.59, and N = 97.

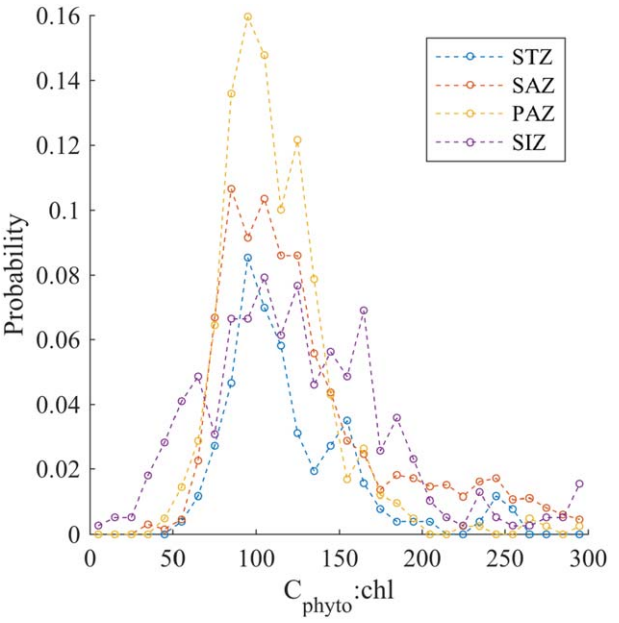

Figure 6. Frequency distribution of phytoplankton carbon (C_{phyto}) to chlorophyll *a* ratio (in g C g chl a^{-1}) from all the SOCCOM and pre-SOCCOM floats grouped by regions. From North to South the regions are Subtropical Zone (STZ), Subantarctic Zone (SAZ), Polar Antarctic Zone (PAZ), and sea ice zone (SIZ).

Johnson et al. [2013, Figure 1], and Figure 1 in this paper). *Marrari et al*. [2006] compared chl *a* from fluorometers calibrated with HPLC with chl *a* from SeaWiFS estimated with OC4v4. They concluded that no significant bias was observed, which is similar to what we find here with MODIS and VIIRS. The data set presented here shows small biases between regions of the SO, however, more matchups are needed to address spatial and temporal biases. Those biases may be related to specific physiological state and species composition as *Dierssen* [2010] and the *IOCCG* [2015] report suggest.

In this analysis, we assume the ratio of chl *a* to fluorescence yield (fl) to be constant (Figure 3), however, the variability is large in the world ocean [*Cullen*, 1982; *Roesler et al*., 2017]. Phytoplankton acclimate to light intensity, nutrient concentrations, trace metals concentrations, and extremely cold temperatures [*Cullen*, 2015; *Behrenfeld et al*., 2005; *Dierssen*, 2010] by changing their intercellular chl *a* concentration and their fluorescence yield. In addition, this ratio also varies with species composition [*Proctor and Roesler*, 2010]. Variability in the chl *a*:fl ratio could, potentially, be modeled with parameters such as PAR, temperature, day of the year, and nutrient concentration in order to enhance our measurements of phytoplankton biomass with both autonomous platforms and satellites.

Nonphotochemical quenching NPQ corrections [*Sackmann et al*., 2008; *Xing et al*., 2012] used to produce our float data set [*Johnson et al*., 2017] could introduce significant uncertainty in the chl *a* concentration estimated from the fluorometers. However, we find that removing the NPQ corrected data from the relation with HPLC chl *a* (used here) changed the slope factor by less than 10%, suggesting that NPQ does not bias the observed relationship. Moreover, no significant bias was observed comparing day-time measurements (NPQ corrected) of chl *a* by floats against OCI chl *a* with nighttime ones (slopes of 0.89 and 1.10, respectively). However, day-time (NPQ corrected) concentrations of chl *a* are slightly offset (overestimate of 21% by OCI). The quality of both relationships could potentially be improved by using mechanistic models or by using a radiometer in addition to the chl *a* fluorometer to compute chl *a* [*Xing et al*., 2011]. Such radiometers are recommended for BGC floats [*Johnson and Claustre*, 2016].

To test whether the float data set is biased, we use an independent data set of 6242 HPLC samples from 1682 profiles between October 1995 and April 2011 from NASA's SeaBASS database (all the data available on 1 February 2017, south of 30°S) is to compare with MODIS OCI matchups (no image available for VIIRS). Out of the 659 matchups, only 97 respected the criteria we used here (Figure 5). The slope of the regression between the in situ and OCI chl *a* is similar to the one obtained with the float comparison, which supports the relationship developed in Figure 3.

The comparison between OC and float POC (Figure 4) is likely biased, as our in situ POC measurements include some dissolved organic material (DOC) adsorbed by the filter which should result in an overestimation of the POC product estimated for the float. A recent analysis (I. Cetinić, personal communication, 2016) suggests, for the amount of water filtered, a likely bias of 33–38 ($\pm$1.3) mg m^{-3}. On the other hand, frequency distributions of float POC overall underestimated the POC concentration (Figure 4c), which is inconsistent with the argument above.

The ratio of chl *a* to phytoplankton carbon (C_{phyto}) is compared to previous studies to further validate our float data set. C_{phyto} is computed with the method from *Graff et al*. [2015] based on $b_{bp}(470)$.The shift in particulate backscattering wavelength is estimated with $b_{bp}(\lambda)=b_{bp}(700)\left(\frac{\lambda}{700}\right)^{-\gamma}$, with $\gamma=0.78$ [*Boss et al*., 2013] assuming a spectrally invariant particulate backscattering ratio. The C_{phyto}:chl *a* computed is consistent with the range (20 to >200 g C g chl a^{-1}) observed for phytoplankton cultures [e.g., *Taylor et al*., 1997], the range (75–250 g C g chl a^{-1}) inferred for the SO by *Behrenfeld et al*. [2005], and broader than the range (20–100 g C g chl a^{-1}) of *Thomalla et al*. [2017] for the SO (Figure 6). Consistent with *Reynolds et al*. [2001] who observed a larger b_{bp}:chl *a* ratio in the SIZ, we observe a similar trend in the C_{phyto}:chl *a*.

5. Conclusion

Our results support the use of the OCI algorithm in the SO. OCI, the default algorithm to estimate chl *a* from NASA, performs well in the SO (average bias of 9% and 12% for VIIRS and MODIS, respectively) and suggests that no specific algorithms is required for this region. With our data set, OCI performs better than SO-specific algorithms in the SIZ (offset of ∼20% for OCI and ∼45% for SPGANTv4). This might be explained by the subregion and seasons used to develop these algorithms (not representative of the whole SIZ), however, more matchups are needed to better constrain the relationship. While float data have significant uncertainties in estimating chl *a* and POC, the large dynamic range in the SO and consistency in the data support the use of profiling floats for validation of satellite-based biogeochemical algorithm performance. POC derived from MODIS and VIIRS agrees well with the float product within the uncertainty specified. The biogeochemical data set from our pre-SOCCOM and SOCCOM autonomous floats are consistent with OC products (chl *a*, POC) and can be used as the third dimension (depth) and provide winter coverage to complement remote sensing in the Southern Ocean.

Acknowledgments
We thank the SOCCOM community for their amazing work and for providing the data set used in this study, as well as Stephen Riser and Ken Johnson for the pre-SOCCOM data set, the many colleagues who helped with shipboard sampling, and analysis by SIO, CSIRO, UCSB, and NASA Ocean Biology and Biogeochemistry group. We thank Ryan Weatherbee for helping to process satellite imagery and useful comments from Magdalena Carranza and Sarah Gille as well as Andrew Thomas for comments on an earlier version of this manuscript. We also thank Dana Swift for integration of optical sensors and dark values measurement. We thank Mati Kahru and B. Greg Mitchell for valuable discussions and help with SPGANT. We thank our reviewers, Pete Strutton and Toby K. Westberry for constructive comments on the manuscript. SOCCOM is supported by the National Science Foundation (NSF), Division of Polar Programs under NSF Award PLR-1425989, with additional support from NOAA US Argo biology and biogeochemistry program supplying profiling floats, and NASA grant NNX14AP49G and NNX15AC08G supplying bio-optical sensors for the SOCCOM floats and supporting the current work. Logistical support for this project in Antarctica was provided by the U.S. National Science Foundation through the U.S. Antarctic Program. We acknowledge NASA Goddard Space Flight Center, Ocean Ecology Laboratory, and Ocean Biology Processing Group for making and sharing Ocean Color data from MODIS and VIIRS Reprocessing 2014.0 [*NASA Goddard Space Flight Center et al*., 2014, 2015]. Float data used in the paper are available at http://www3.mbari.org/soccom/SOCCOM_Data_Archive/Floats_LoResQC_28-Nov2016.zip and are processed according to *Johnson et al*. [2017]. MODIS and VIIRS images level 2 are available at https://oceandata.sci.gsfc.nasa.gov. The HPLC data set used in the discussion is available on SeaBASS (https://seabass.gsfc.nasa.gov/search) using the filters: date measured = 1930–01-01 to 2017–02-01; data archived = 2000–01-01 to 2017–02-01; North = −30; South = −90; West = −180; East = 180; Products = HPLC.

References

Bailey, S. W., and P. J. Werdell (2006), A multi-sensor approach for the on-orbit validation of ocean color satellite data products, *Remote Sens. Environ.*, *102*(1–2), 12–23, doi:10.1016/j.rse.2006.01.015.

Behrenfeld, M. J., E. Boss, D. A. Siegel, and D. M. Shea (2005), Carbon-based ocean productivity and phytoplankton physiology from space, *Global Biogeochem. Cycles*, *19*, GB1006, doi:10.1029/2004GB002299.

Behrenfeld, M. J., et al. (2016), Annual boom-bust cycles of polar phytoplankton biomass revealed by space-based LiDAR, *Nat. Geosci.*, *10*(2), 118–122, doi:10.1038/ngeo2861.

Boss, E., M. Picheral, T. Leeuw, A. Chase, E. Karsenti, G. Gorsky, L. Taylor, W. Slade, J. Ras, and H. Claustre (2013), The characteristics of particulate absorption, scattering and attenuation coefficients in the surface ocean; contribution of the Tara Oceans expedition, *Methods Oceanogr.*, *7*, 52–62, doi:10.1016/j.mio.2013.11.002.

Cullen, J. J. (1982), The deep chlorophyll maximum: Comparing vertical profiles of chlorophyll, *Deep Sea Res., Part B*, *29*(12), 787, doi:10.1016/0198-0254(82)90274-6.

Cullen, J. J. (2015), Subsurface chlorophyll maximum layers: Enduring enigma or mystery solved?, *Annu. Rev. Mar. Sci.*, *7*(1), 207–239, doi:10.1146/annurev-marine-010213-135111.

Dierssen, H. M. (2010), Perspectives on empirical approaches for ocean color remote sensing of chlorophyll in a changing climate, *Proc. Natl. Acad. Sci.*, *107*(40), 17,073–17,078, doi:10.1073/pnas.0913800107.

Dierssen, H. M., and R. C. Smith (2000), Bio-optical properties and remote sensing ocean color algorithms for Antarctic Peninsula waters, *J. Geophys. Res.*, *105*(C11), 26,301–26,312, doi:10.1029/1999JC000296.

Frölicher, T. L., J. L. Sarmiento, D. J. Paynter, J. P. Dunne, J. P. Krasting, and M. Winton (2015), Dominance of the Southern Ocean in Anthropogenic carbon and heat uptake in CMIP5 models, *J. Clim.*, *28*(2), 862–886, doi:10.1175/JCLI-D-14-00117.1.

Gordon, H. R., and D. K. Clark (1980), Remote sensing optical properties of a stratified ocean: An improved interpretation, *Appl. Opt.*, *19*(20), 3428, doi:10.1364/AO.19.003428.

Graff, J. R., T. K. Westberry, A. J. Milligan, M. B. Brown, G. Dall'Olmo, V. van Dongen-Vogels, K. M. Reifel, and M. J. Behrenfeld (2015), Analytical phytoplankton carbon measurements spanning diverse ecosystems, *Deep Sea Res., Part I*, *102*, 16–25, doi:10.1016/j.dsr.2015.04.006.

Guinet, C., et al. (2013), Calibration procedures and first dataset of Southern Ocean chlorophyll *a* profiles collected by elephant seals equipped with a newly developed CTD-fluorescence tags, *Earth Syst. Sci. Data*, *5*(1), 15–29, doi:10.5194/essd-5-15-2013.

Hu, C., Z. Lee, and B. Franz (2012), Chlorophyll *a* algorithms for oligotrophic oceans: A novel approach based on three-band reflectance difference, *J. Geophys. Res.*, *117*, C01011, doi:10.1029/2011JC007395.

IOCCG (2011), Bio-optical sensors on Argo floats, in *Reports of the International Ocean-Colour Coordinating Group, No. 11*, edited by H. Claustre, Dartmouth, Canada.

IOCCG (2015), Ocean colour remote sensing in polar seas, in *IOCCG Report Series, No. 16*, edited by M. Babin et al., Dartmouth, Canada.

Johnson, K., and H. Claustre (2016), The scientific rationale, design, and implementation plan for a Biogeochemical-Argo float array, *Biogeochem.-Argo Plann. Group*, *58*, doi:10.13155/46601. [Available at http://archimer.ifremer.fr/doc/00355/46601/.]

Johnson, R., P. G. Strutton, S. W. Wright, A. McMinn, and K. M. Meiners (2013), Three improved satellite chlorophyll algorithms for the Southern Ocean, *J. Geophys. Res. Oceans*, *118*, 3694–3703, doi:10.1002/jgrc.20270.

Johnson, K. S., et al. (2017), Biogeochemical sensor performance in the SOCCOM profiling float array, *J. Geophys. Res. Oceans*, *122*, doi:10.1002/2017JC012838.
Kahru, M., and B. G. Mitchell (2010), Blending of ocean colour algorithms applied to the Southern Ocean, *Remote Sens. Lett.*, *1*(2), 119–124, doi:10.1080/01431160903547940.
Marrari, M., C. Hu, and K. Daly (2006), Validation of SeaWiFS chlorophyll *a* concentrations in the Southern Ocean: A revisit, *Remote Sens. Environ.*, *105*(4), 367–375, doi:10.1016/j.rse.2006.07.008.
Mitchell, B. G., and O. Holm-Hansen (1991), Bio-optical properties of Antarctic Peninsula waters: Differentiation from temperate ocean models, *Deep Sea Res., Part A*, *38*(8–9), 1009–1028, doi:10.1016/0198-0149(91)90094-V.
Mitchell, B. G., and M. Kahru (2009), Bio-optical algorithms for ADEOS-2 GLI, *J. Remote Sens. Soc. Jpn.*, *29*(1), 80–85, doi:10.11440/rssj.29.80.
Mobley, C. D., J. Werdell, B. Franz, Z. Ahmad, and S. Bailey (2016), *Atmospheric Correction for Satellite Ocean Color Radiometry, A Tutorial and Documentation*, NASA Ocean Biol. Process. Group, NASA Goddard Space Flight Cent., Greenbelt, Md.
Mueller, J. L., R. R. Bidigare, C. Trees, W. M. Balch, J. Dore, D. T. Drapeau, D. M. Karl, L. Van Heukelem, and J. Perl (2003), Ocean optics protocols for satellite ocean color sensor validation, Revision 5, vol. V, Biogeochemical and bio-optical measurements and data analysis protocols, *NASA Tech. Memo. V(2003–211621, Rev. 5, vol. V)*, 36 pp., NASA Goddard Space Flight Cent., Greenbelt, Md
NASA Goddard Space Flight Center, Ocean Ecology Laboratory, and Ocean Biology Processing Group (2014), *MODIS-Aqua Level-2 Ocean Color Data Version 2014*, Greenbelt, Md., doi:10.5067/AQUA/MODIS_OC.2014.0.
NASA Goddard Space Flight Center, Ocean Ecology Laboratory, and Ocean Biology Processing Group (2015), *VIIRS-NPP Level 2 Ocean Color Data Version 2014*, Greenbelt, Md., doi:10.5067/NPP/VIIRS/L2/OC/2014.
Orsi, A. H., T. Whitworth, and W. D. Nowlin (1995), On the meridional extent and fronts of the Antarctic Circumpolar Current, *Deep-Sea Res., Part I*, *42*, 641–673.
Proctor, C. W., and C. S. Roesler (2010), New insights on obtaining phytoplankton concentration and composition from in situ multispectral chlorophyll fluorescence, *Limnol. Oceanogr. Methods*, *8*, 695–708, doi:10.4319/lom.2010.8.695.
Reynolds, R. A., D. Stramski, and B. G. Mitchell (2001), A chlorophyll-dependent semianalytical reflectance model derived from field measurements of absorption and backscattering coefficients within the Southern Ocean, *J. Geophys. Res.*, *106*(C4), 7125–7138, doi:10.1029/1999JC000311.
Ricker, W. E. (1973), Linear regressions in fishery research, *J. Fish. Res. Board Can.*, *30*(3), 409–434, doi:10.1139/f73-072.
Roemmich, D., and J. Gilson (2009), The 2004–2008 mean and annual cycle of temperature, salinity, and steric height in the global ocean from the Argo Program, Prog. *Oceanogr.*, *82*, 81–100.
Roesler, et al. (2017), Recommendations for obtaining unbiased chlorophyll estimates from in situ chlorophyll fluorometers: A global analysis of WET Labs ECO sensors, *Limnol. Oceanogr. Methods*, *15*, 572–585, doi:10.1002/lom3.10185.
Sackmann, B. S., M. J. Perry, and C. C. Eriksen (2008), Seaglider observations of variability in daytime fluorescence quenching of chlorophyll-*a* in Northeastern Pacific coastal waters, *Biogeosci. Discuss.*, *5*(4), 2839–2865, doi:10.5194/bgd-5-2839-2008.
Sarmiento, J. L., et al. (2004), Response of ocean ecosystems to climate warming, *Global Biogeochem. Cycles*, *18*, GB3003, doi:10.1029/2003GB002134.
Stramski, D., et al. (2008), Relationships between the surface concentration of particulate organic carbon and optical properties in the eastern South Pacific and eastern Atlantic Oceans, *Biogeosciences*, *5*(1), 171–201, doi:10.5194/bg-5-171-2008.
Sullivan, C. W., K. R. Arrigo, C. R. McClain, J. C. Comiso, and J. Firestone (1993), Distributions of phytoplankton blooms in the Southern Ocean, *Science*, *262*(5141), 1832–1837, doi:10.1126/science.262.5141.1832.
Sullivan, J. M., M. S. Twardowski, J. Ronald, V. Zaneveld, and C. C. Moore (2013), Measuring optical backscattering in water, in *Light Scattering Reviews 7, Springer Praxis Books*, edited by A. A. Kokhanovsky, pp. 189–224, Springer, Berlin, doi:10.1007/978-3-642-21907-8_6.
Taylor, A., R. Geider, and F. Gilbert (1997), Seasonal and latitudinal dependencies of phytoplankton carbon-to-chlorophyll *a* ratios: Results of a modelling study, *Mar. Ecol. Prog. Ser.*, *152*(1–3), 51–66, doi:10.3354/meps152051.
Thomalla, S. J., A. G. Ogunkoya, M. Vichi, and S. Swart (2017), Using optical sensors on gliders to estimate phytoplankton carbon concentrations and Chlorophyll-to-carbon ratios in the Southern Ocean, *Frontiers Mar. Sci.*, *4*, 1–19, doi:10.3389/fmars.2017.00034.
Werdell, P. J., and S. W. Bailey (2005), An improved in-situ bio-optical data set for ocean color algorithm development and satellite data product validation, *Remote Sens. Environ.*, *98*(1), 122–140, doi:10.1016/j.rse.2005.07.001.
Xing, X., A. Morel, H. Claustre, D. Antoine, F. D'Ortenzio, A. Poteau, and A. Mignot (2011), Combined processing and mutual interpretation of radiometry and fluorimetry from autonomous profiling Bio-Argo floats: Chlorophyll *a* retrieval, *J. Geophys. Res.*, *116*, C06020, doi:10.1029/2010JC006899.
Xing, X., H. Claustre, S. Blain, F. D'Ortenzio, D. Antoine, J. Ras, and C. Guinet (2012), Quenching correction for in vivo chlorophyll fluorescence acquired by autonomous platforms: A case study with instrumented elephant seals in the Kerguelen region (Southern Ocean), *Limnol. Oceanogr. Methods*, *10*(7), 483–495, doi:10.4319/lom.2012.10.483.
Xing, X., H. Claustre, E. Boss, C. Roesler, E. Organelli, A. Poteau, M. Barbieux, and F. D'Ortenzio (2017), Correction of profiles of in-situ chlorophyll fluorometry for the contribution of fluorescence originating from non-algal matter, *Limnol. Oceanogr. Methods*, *15*(1), 80–93, doi:10.1002/lom3.10144.
Zaneveld, J. R. V., A. H. Barnard, and E. Boss (2005), Theoretical derivation of the depth average of remotely sensed optical parameters, *Opt. Express*, *13*(22), 9052, doi:10.1364/OPEX.13.009052.
Zhang, X., L. Hu, and M.-X. He (2009), Scattering by pure seawater: Effect of salinity, *Opt. Express*, *17*(7), 5698–5710, doi:10.1364/OE.17.012685.